Applied Surface Science 546 (2021) 148835

Contents lists available at ScienceDirect

Applied Surface Science

journal homepage: www.elsevier.com/locate/apsusc

Full Length Article

A promising Zn-Ti layered double hydroxide/Fe-bearing montmorillonite composite as an efficient photocatalyst for Cr(VI) reduction: Insight into the role of Fe impurity in montmorillonite

Chitiphon Chuaicham [a,*], Yihuang Xiong [b], Karthikeyan Sekar [a], Weinan Chen [b], Li Zhang [a], Bunsho Ohtani [c], Ismaila Dabo [b], Keiko Sasaki [a,c,*]

[a] Department of Earth Resources Engineering, Kyushu University, Fukuoka 819-0395, Japan
[b] Department of Materials Science and Engineering, The Pennsylvania State University, University Park, PA 16802, United States
[c] Institute for Catalysis, Hokkaido University, Sapporo 001-0021, Japan

ARTICLE INFO

Keywords:
Photocatalyst
Montmorillonite
Layered double hydroxide
Cr(VI) reduction

ABSTRACT

Zn-Ti layered double hydroxide/montmorillonite (ZTL/MT) and Fe-doped ZTL/MT (ZTL/Fe@MT20%) were prepared as photocatalyst for Cr(VI) reduction. The ZTL/Fe@MT20% exhibited the highest photocatalytic activity, suggesting that a combination of ZTL and Fe-bearing MT could enhance photocatalytic activity by suppressing the recombination of photogenerated electron-hole pairs. On the basis of electronic-structure calculations, a photocatalytic mechanism for Cr(VI) reduction and the effect of Fe^{3+} on the structure of MT in ZTL/MT composites is proposed by density functional theory approach, whereby Fe impurities in MT generate a new mid-gap state that induce a Z-scheme heterojunction with ZTL, leading to reduced recombination of the photogenerated charge carriers in ZTL. These results establish that MT can not only act as a support material but also play an important role for photocatalytic reaction when Fe impurities are present in its structure.

1. Introduction

Hexavalent chromium is a primary health concern due to its high carcinogenic and mutagenic potentials when present in waters and soils as a result of anthropogenic emissions [1]. According to guidelines from the World Health Organization, chromium concentration must be brought down below 0.1 mg/L to comply with drinking water standards [2]. An effective remediation strategy for the treatment of aqueous chromium consists of reducing hexavalent chromium (Cr(VI)) to trivalent chromium (Cr(III)), thereby enabling its precipitation into hydroxides in moderately acidic or alkaline environments [3].

The reduction of Cr(VI) can be conventionally achieved by chemical [4], electrochemical [5], or biological means [6]. In addition, various physical separation methods have been used for the treatment of toxic Cr (VI) in an aqueous solution, such as surface immobilization and membrane filtration [7]. Nevertheless, all these techniques have significant drawbacks, including high operating costs, incomplete treatment of the pollutants, limited industrial scalability, and adverse environmental effects [2]. In light of these problems, photocatalysis has emerged in recent years as a technically attractive solution for the reductive precipitation of Cr(VI)-containing species. The central challenge facing photocatalytic chromium reduction is the development of photoactive semiconductors compatible with the solar spectrum and band edges aligned with the redox potentials for Cr(VI)/Cr(III). Previously, there are many potential materials were used as photocatalyst for reduction of Cr (VI) such as metal oxides (TiO_2, ZnO, Fe_2O_3, CoO, ThO_2, CeO_2, Bi_2WO_6), metal sulfide ($InSnS_2$, CdS, ZnS, Bi_2S_3), bismuth oxyhalides (BiOBr, BiOCl, BiOI) and organic photocatalyst (C_3N_4) [8,9,10,11,12,13,14,15,16,17,18,19,20,21]. However, some disadvantages remain in the single-catalyst system for instance high recombination of photogenerated charge carriers, low electrical conductivity, less light absorption ability in the solar light region, require a relatively high amount of catalyst. Also, the low stability of photocatalyst in acidic condition is one of drawback because the photocatalytic reduction of Cr (VI) usually carry out in acid pH to achieve the high efficiency [22]. Thus, the search of other material or development of new composite which has high stability and activity could be interest for improving the reduction of Cr(VI) by photocatalysis. Moreover, photocatalytic conditions such as catalyst loading, reaction temperature, addition of hole scavenger, pH have been investigated to achieve the highest reduction

* Corresponding authors.
E-mail addresses: chitiphon.c@gmail.com (C. Chuaicham), keikos@mine.kyushu-u.ac.jp (K. Sasaki).

https://doi.org/10.1016/j.apsusc.2020.148835
Received 22 October 2020; Received in revised form 26 November 2020; Accepted 21 December 2020
Available online 28 December 2020

efficiency.

Layered double hydroxides (LDH) have been proposed as promising candidates for the photocatalytic decomposition of organic pollutants and the light-assisted removal of heavy metals from wastewaters. LDH are two-dimensional anionic clays of generic chemical formula $[M^{2+}_{1-x}M^{3+}_{x}(OH)_2]^{z+}(A^{n-})_{z/n}\cdot yH_2O$, where M is metal cations and A is the interlayer anion compensating for the positive charge of the layers [23,24]. From previous works, Zn-Ti LDH (ZTL) has been reported the higher photocatalytic efficiency for wastewater treatment and water splitting than among of LDH photocatalysts [25–31]. However, the performance of these compounds is limited by electron-hole recombination [27]. To solve the problem, the formation of heterojunction between LDH and metal oxides is an effective approach to prevent the recombination of photogenerated charge carriers [32–34]. Das and coworkers found that Au-loaded $CaFe_2O_4$/CoAl LDH p-n junctions exhibited high photocatalytic activity for chromium reduction [35]. Yuan and coworkers developed mixed metal oxide heterojunctions by calcination of Zn-Al layered double hydroxides, finding that the calcined product displayed excellent photocatalytic activity of Cr(VI) reduction under UV light irradiation [36]. Recently, Li and coworkers reported the synthesis of $Zn_xCd_{1-x}S$ nanoparticles dispersed on CoAl-layered double hydroxide by ultrasonic treatment. The composite exhibited higher hydrogen production compare with pure $Zn_xCd_{1-x}S$ because of improving photoelectron transfer and inhibition of charge recombination by the heterojunction of $Zn_xCd_{1-x}S$ and CoAl-layered double hydroxide [37].

In recent years, montmorillonite (MT)-based composites has attracted much interest as a candidate photocatalyst due to its natural abundance, high two-dimensional surface area, low cost, high chemical stability, low toxicity, and environmental compatibility. Multiple reports have examined the enhanced photocatalytic performance of MT composites [38–40]; however, the mechanisms at the origins of this improved photocatalytic activity remain poorly understood. In this work, we undertake a systematic study of a series of ZnTi-LDH/MT composites (ZTL/MT) and ZnTi-LDH/Fe-doped MT (ZTL/Fe@MT), and evaluate their performance for Cr(VI) photoreduction. The extra Fe(III) ions were added to the ZTL/MT complex to reduce the energy band gap and increase the light absorption ability of the MT in the composite. It has been reported that the Fe-dopant in photocatalyst generates the new electronic level which can reduce the energy band gap and inhibit the recombination of photogenerated electron and hole [41–43]. The as-prepared materials were characterized by X-ray powder diffraction (XRD), UV–vis diffuse reflectance spectroscopy (UV–Vis/DRS), photoluminescence spectroscopy (PL), X-ray photoelectron spectroscopy (XPS), and transmission electron microscopy energy-dispersive X-ray spectroscopy (TEM-EDX). The electronic structure of ZTL and Fe-bearing MT were studied using density-functional theory (DFT) to elucidate the charge migration properties in composites.

2. Materials and methods

2.1. Materials and reagents

Montmorillonite (MT, Kunipia-F), which was obtained from Kunimine Industries Co. Ltd., (Tokyo, Japan), has the chemical formula of $(Na_{0.97}Ca_{0.08})^{+1.13}(Si_{7.68}Al_{0.32})(Al_{2.94}Fe^{III}_{0.25}Fe^{II}_{0.03}Mg_{0.78})O_{20}(OH)_4^{-1.13}\cdot nH_2O$, with a cation exchange capacity (CEC) of 1.15 meq/g [44]. Sodium chromate tetrahydrate ($Na_2CrO_4\cdot 4H_2O$), zinc nitrate hexahydrate ($Zn(NO_3)_2\cdot 6H_2O$), titanium(IV) chloride ($TiCl_4$) and urea ($CO(NH_2)_2$) were obtained from Wako Chemicals, (Osaka, Japan). All the chemicals were used directly without further purification.

2.2. Preparation of Zn-Ti layered double hydroxides (ZTL)

ZTL with a Zn:Ti molar ratio of 4:1 was synthesized by a co-precipitation refluxing method. Typically, 1.19 g of $Zn(NO_3)_2\cdot 6H_2O$ and 0.22 mL of $TiCl_4$ solution (the $TiCl_4$ solution was prepared mixing 0.11 mL $TiCl_4$ and 0.11 mL of HCl) were dissolved in the 50 mL of deionized water, followed by the addition of 1.5 g of urea. The mixed metal solution was heated under gentle reflux with vigorous stirring at 130 °C for 24 h. The white powders are produced, separated by flirtation and washed with deionized water several times. Finally, the ZTL was obtained by drying at 75 °C for 24 h in an oven.

2.3. Preparation of Zn-Ti layered double hydroxides/montmorillonite composites (ZTL/MT)

ZTL/MT were prepared by a similar refluxing method. Firstly, 1.19 g of $Zn(NO_3)_2\cdot 6H_2O$ and 0.11 mL $TiCl_4$ were added into 50 mL of deionized water, followed by the addition of 1.5 g of urea. The mixed metal solution was heated under gentle reflux with vigorous stirring at 130 °C for 12 h. Different amounts of MT (10, 20 and 30 wt%) were added into the above solutions, followed by ultra-sonication for 3 h. Afterward, the suspended solutions were continuously refluxed for 12 h. The products were collected by filtration and washing with the deionized water several times. Finally, the white colored powders were obtained after drying at 75 °C for 24 h in an oven. The obtained products are denoted as ZTL/MT*X*%, where *X* stands for the calculated weight percent of MT in the composites.

2.4. Preparation of Zn-Ti layered double hydroxides/Fe doped montmorillonite composite (ZTL/Fe@MT20%)

ZTL/Fe@MT20% were prepared by ionic exchange of MT in ZTL/MT20%. Briefly, 0.2 g of ZTL/ MT20% was dispersed in 200 mL 0.015 mM of $Fe(NO)_3\cdot 9H_2O$ (around 0.2 times of CEC of MT in ZTL/ MT20% composite), following by stirring for 10 min at pH 3. Afterward, the products were collected by filtration and washing with the deionized water several times. Finally, the solid powders were obtained after drying at 75 °C for 24 h in an oven.

2.5. Characterizations

The crystal phases of the pristine and synthetic products before and after photocatalytic reduction of Cr(VI) were characterized by powder X-ray diffraction (XRD) on an Ultima IV diffractometer (RIGAKU, Akishima, Japan) using Cu Kα radiation with 40 kV acceleration voltage and 40 mA applied current at a 2°/min scanning speed and 0.02° step sizes. Transmission electron microscopic (TEM) images of as-prepared samples and spent ZTL/MT20% after photocatalytic reduction of Cr (VI) were observed on a transmission electron microscope (JEM-2100HCKM, JEOL; Akishima, Japan). The oxidation states of the samples were investigated by X-ray photoelectron spectroscopy (XPS), ESCA 5800 (ULVAC-PHI, Inc.; Kanagawa, Japan) using a monochromated Al Kα X-ray source at 200 W. The data analysis was performed by the Casa XPS software (version 2.3.12.8). The binding energy was calibrated using the energy reference of E_B [C 1s] = 284.6 eV, assigned to carbon contamination derived from vacuum oil in the apparatus. The band gap energy (E_g) of the as-prepared samples were examined by using UV–Vis diffuse reflectance spectroscopy (UV–Vis/DRS) with a Shimadzu UV-2450 spectrophotometer equipped with ISR-2200 integrating sphere attachment (Kyoto, Japan). Solid-state photoluminescence (PL) spectra of samples were measured using a JASCO F-6600 spectrofluorometer with a 320 nm excitation wavelength and 400–470 emission wavelength. Scanning electron microscopic (SEM) analysis was conducted using a VE-9800 SEM (Keyence, Osaka, Japan) with 20 kV acceleration voltages.

The reverse double beam-photoacoustic spectroscopy (RDB-PAS) technique was utilized for characterizing energy resolved distribution of electron trap (ERDT) patterns of MT, ZTL, ZTL/ MT20% and ZTL/Fe@MT20%. A 200 mg sample was set into a photoacoustic spectroscopy (PAS) cell equipped with an electret condenser microphone and a

quartz window. The upper part under N_2 flow was saturated with methanol vapor for at least 30 min and a light beam from a xenon lamp with a grating monochromator modulated at 80 Hz. A light chopper was irradiated from 650 nm to 350 nm through the cell window to detect the PAS signal using a digital lock-in amplifier, and the photoacoustic (PA) spectra were recorded to obtain a PA spectrum of graphite for calibration. The ERDT pattern was obtained by determining the change in photo-absorption for the accumulated electrons.

2.6. Electronic-structure calculations

We performed self-consistent-field calculations with the PW code of the open-source Quantum-Espresso software [45]. All the calculations were carried out at the semilocal Perdew-Burke-Ernzerhof level [46], with van der Waals corrections following the DFT-D parameterization of long-range interactions between fluctuating dipoles. The ionic cores were represented by ultrasoft pseudopotentials. Kinetic energy cutoffs were set to 60 and 480 Ry for the reciprocal-space expansion of the wave functions and charge density, respectively. A Marzari-Vanderbilt smearing [47] of 0.005 Ry was employed for the sampling of the Brillouin zone with 6 × 4 × 4 and 4 × 8 × 4 Monkhorst-Pack grids for the ZTL and Fe-bearing MT, respectively. The Hubbard *U* correction was applied to the Ti and Fe sites to account for electron correlations (U_{Ti} = 6.0 eV and U_{Fe} = 1.9 eV). Atomic positions and lattice vectors were optimized for both ZTL and Fe-bearing MT until the residual force on each atom was smaller than 0.01 eV/Å and the residual pressure was lower than 0.5 kbar.

2.7. Photocatalytic test

Photocatalytic activity tests were performed to evaluate the reduction of Cr(VI). In a typical procedure, 50 mg of synthesized composites were dispersed in the 50 mL of 10 ppm of Cr(VI) aqueous solution under dark conditions for 30 min to reach adsorption–desorption equilibrium. The pH of the suspension solutions was adjusted by 0.5 M HCl and 0.5 M NaOH in order to maintain pH 3 before the photocatalytic reaction. Then, the suspensions were irradiated using a 500 W Xe lamp with light intensity around 83 mW/cm^2. During the illumination, the suspensions were taken out and filtrated by 0.45 μm membrane filters to separate the synthesized composites. The remaining concentrations of Cr(VI) were determined by a diphenyl carbazide colorimetric method by a UV–Vis spectrometer at 554 nm [48].

3. Results and discussion

3.1. Characterizations

Fig. 1 shows the XRD patterns of MT, ZTL, ZTL/MT composites and ZTL/Fe@MT20%. It can be seen that ZTL showed a strong diffraction peak at 2θ = 13.2°, which is attributed to the 003 basal plane of LDH. The observed basal reflection of the 003 basal plane with interlayer distance 0.66 nm of ZTL is similar to previous report of the Zn-Ti LDH [27,29,49]. Compared with other LDH, the 003 basal plane of ZTL show a little shift to a higher angle compared with other reported LDH such as Mg-Al LDH, suggesting that the incorporation of Ti(VI) in Zn-Ti LDH cause the decreasing of interlayer distance with similar with the previous report [27]. Also, the small interlayer distance of the 003 basal plane of ZTL confirmed the intercalation of carbonate ion (CO_3^{2-}) between the LDH sheets [49]. Moreover, the other peaks located at 2θ angles of 24.3°, 35.4°, 31.2°, 33.0°, 36.1°, 39.0°, 47.7°, 54.3°, 58.6°, 59.5°, and 63.3°, correspond to the planes 006, 012, 100, 101, 009, 107, 108, 01$\underline{11}$, 110, 113 and 10$\underline{13}$ respectively, which are associated to the Zn-Ti LDH phase in previous reports [27,50].

The diffraction peaks of ZTL/MT with different MT contents and Fe doped MT/ZTL composite (ZTL/Fe@MT20%) resemble those of ZTL, indicating that the presence of MT in the composite does not change the

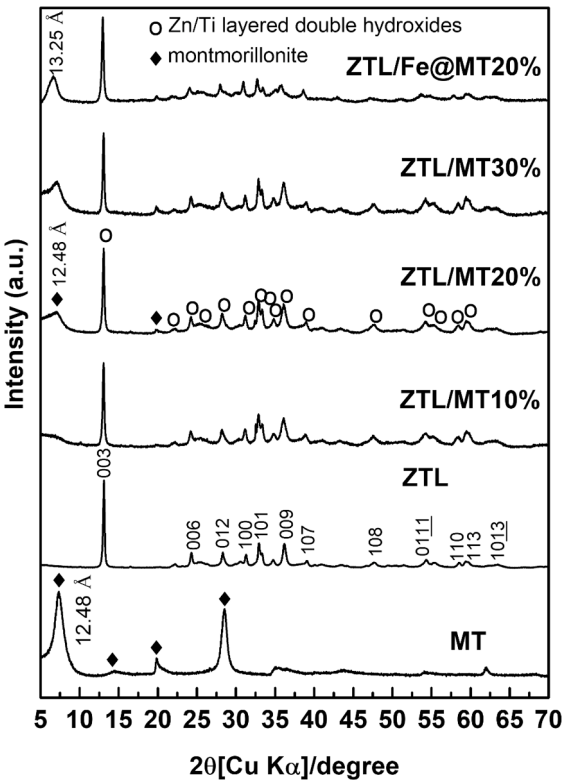

Fig. 1. XRD patterns of MT, ZTL, ZTL/MT composites and ZTL/Fe@MT20%.

backbone structure of the ZTL. The MT exhibits five strong diffraction peaks at 7.3°, 19.8°, 28.6°, 35.0°, and 61.9°, which correspond to the 001, 100, 004, 110 and 300 planes. As for the ZTL/MT composite, a broad peak can be found at 2θ = 7.3°, and the peak intensity becomes stronger with increasing MT content. However, the main diffraction peak of 001 plan of MT in the ZTL/Fe@MT20% shifted to lower diffraction angle, indicating that the additional Fe might intercalate between the layer of MT, leading to expand the interlayer spacing of MT from 12.48 to 13.25 Å.

To investigate the electronic and optical properties of MT, ZTL, ZTL/MT composites and ZTL/Fe@MT20%, UV–Vis diffuse reflectance spectra (DRS) were collected, as shown in Fig. 2**a**. The absorption spectra of the MT, ZTL and composites showed the strong absorption of light in the 300–400 nm region, suggesting the ZTL and composites can be activated by UV light. Compared to ZTL, the ZTL/MT composites and ZTL/Fe@MT20% exhibited higher light absorption ability in the UV and visible light region. Also, the bandgap energy (*Eg*) of the MT, ZTL, ZTL/MT composites, and ZTL/Fe@MT20% were determined using the Tauc's equation, **Eq. (1)**:

$$(\alpha h\nu)^{1/n} = A(h\nu - E_g) \quad (1)$$

where *α, h, ν, Eg*, and *A* are t absorption (extinction) coefficient, Planck's constant, light frequency, bandgap energy, and the proportionality constant, respectively [27,51]. In **Eq. (1),** the exponent *n* is dependent on the type of optical transition: $n = 2$ for the indirect allowed transitions and $n = 1/2$ for the direct allowed transitions. From **Eq. (1)**, the photon energy ($h\nu$) was converted from the photon wavelength (λ)**.** Also, the observed absorbance (α) of samples was multiplied with $h\nu$ to get $\alpha h\nu$, following by taking the square root of the obtained $\alpha h\nu$ to obtain $(\alpha h\nu)^{1/2}$. The *Eg* is estimated by extrapolating the linear portion of the plot of $(\alpha h\nu)^{1/2}$ versus $h\nu$ to y-axis = 0 to get the *Eg* value as shown in Fig. 2**b**. It can be seen that the multiple transition states of MT can be observed around 2.56, and 3.72 eV. These transitions might be due to the middle gap state which was generated from impurities in the MT

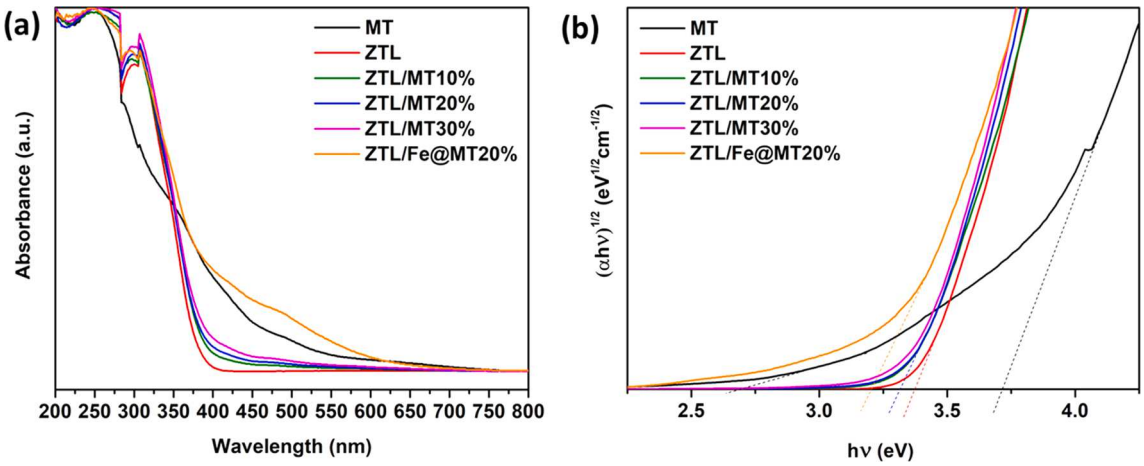

Fig. 2. (a) UV–vis diffuse reflectance spectra and (b) Tauc spectra bandgap (Eg) analyses of MT, ZTL, ZTL/MT composites and ZTL/Fe@MT20%.

structure. The *Eg* of ZTL, ZTL/MT10%, ZTL/MT20%, ZTL/MT30% and ZTL/Fe@MT20% were estimated to be 3.41, 3.36, 3.34, 3.33 and 3.25 eV, respectively, lower than that of the as-prepared ZTL. Thus, the formation of a heterojunction between ZTL and Fe-bearing MT or Fe doped MT provides higher light absorption ability and lower band gaps, implying that the composites could generate more electron-hole pairs under illumination, which might play an important role for the reduction of Cr(VI).

Additionally, ICP-OES and XRF techniques were used to confirm the present of Fe in ZTL/MT20%. The ICP-OES result showed the negligibly remaining of Fe ions in the synthesis solution around $7x10^{-6}$ mM (less than 1% of adding Fe ions), indicating that all of added Fe ions were included into the MT in ZTL/MT20% that is in good agreement with the increasing of Fe content of ZTL/Fe@MT20% compared with ZTL/MT20% using XRF analysis (**Table S1**). Also, the Fe impurities in MT were observed, potentially affecting the optical and photocatalytic properties of the ZTL/MT composites.

Fig. S1a and S1b present the typical dark-field and bright-field TEM images of ZTL/Fe@MT20%. It is clear that the ZTL/Fe@MT20% composite shows low crystallinity over several hundreds of nanometers. The locations of Fe in the composite were further confirmed by TEM-EDX elemental mapping. As illustrated in **Fig. S1e**, the mapping results show that O, Zn, and Ti are predominant components in the ZTL/Fe@MT20% composite, which can be ascribed to ZTL. Meanwhile, Al, Si, and Mg elements are homogeneously distributed and overlapped with the ZTL throughout the whole composite. Moreover, the location of Fe is mainly overlap with Mg, indicating the present of Fe in the MT structure. These observations confirm the formation of interface between ZTL and Fe doped MT.

The morphology of pure MT, ZTL and the composites were investigated using scanning electron microscopy (SEM) and the results were shown in **Fig. S2**. It can be seen that the pure MT showed a sheet-like structure with smooth surface, while ZTL exhibited plate-like morphology with smaller particles, comparing with MT. The morphology of ZTL/MT composites displayed the combination of small ZTL particles on the surface MT, which is expected from an ideal composite structure. Moreover, the addition of extra Fe(III) ions in ZTL/Fe@MT20% sample did not change the morphology of the ZTL/MT20% composite, indicating that the extra Fe(III) ions might penetrate to MT structure in ZTL/MT20% by the cationic exchange process. The SEM result of ZTL/Fe@MT20% is in good agreement with the high magnification of TEM observation of this sample as shown in **S1c, d.** The TEM results clearly show a combination between small dark particles of ZTL contract with the large bright particle of MT, confirming the heterojunction between ZTL and MT was formed under synthesis.

The surface chemical composition and oxidation states of Zn, Ti and Fe in MT, ZTL, ZTL/MT20% and ZTL/Fe@MT20% were investigated by XPS, as shown in Fig. 3. As can be seen in Fig. 3**a**, the XPS spectra of ZTL, ZTL/MT20% and ZTL/Fe@MT20% show a binding energy at E_B[Zn $2p_{3/2}$] around 1021.5 eV, which can be attributed to Zn(II). Meanwhile, high-resolution XPS for Ti 2p of ZTL, ZTL/MT20% and ZTL/Fe@MT20% (Fig. 3**b**) shows a binding energy at E_B[Ti $2p_{3/2}$] about 457.1 eV, assigned to Ti(IV). In Fig. 3**c,** the peak of low intensity at 712.9 eV of MT, ZTL/MT20% and ZTL/Fe@MT20% can be assigned to Fe $2p_{3/2,}$ confirming the presence of Fe(III) in low concentration in the samples. Furthermore, the valence band (VB) of ZTL and MT were investigated in order to elucidate the photocatalytic pathway in ZTL/MT. The measured XPS VB potential for ZTL and MT **(**Fig. 3**d)** are of 1.44 eV and 2.70 eV, respectively. According to their *Eg*, the conduction bands (CB) of ZTL and MT are calculated to be at −1.97 eV and −1.08 eV, respectively.

In addition, the surface electronic properties of MT, ZTL, ZTL/MT20% and ZTL/Fe@MT20% were investigated using RDB-PAS. The energy-resolved distribution of electron traps combined conduction band bottom (ERDT/CBB) results from RDB-PAS can reflect the surface properties of photocatalyst, which might have relationship with photocatalytic activity [52,53]. Fig. 4 shows the ERDT/CBB patterns for MT, ZTL, ZTL/MT20% and ZTL/Fe@MT20% plotted as a function of energy from the valence bond top (VBT) vs. electron-trap density. It was clear that MT has no electron trap (ETs) due to it has a larger energy band gap and contains some amount of water in the structure of MT which can interfere the RDB-PAS measurement. However, the accumulation of electron patterns can be observed around energy ranges of 2.2–3.0 eV for ZTL, ZTL/MT20% and ZTL/Fe@MT20%, indicating that the ZTL and the composites have ETs located on the surface near CBB to accept electron from VBT. Compared with ERDT/ CBB of ZTL, the shape and total electron density of ZTL/MT20% and ZTL/Fe@MT20% are similar to that of ZTL, indicating that the ZTL is formed at the outer surface of MT and the introduction of MT or Fe in the composites do not change the surface electronic properties ZTL.

It is known that photocatalytic processes are strongly limited by the recombination of the photogenerated charge carriers and heterojunctions can avoid these recombination processes to increase the lifetime of excited electrons. Here, photoluminescence analysis (PL) is used to measure the recombination kinetics of the electron-hole pairs. As can be seen from Fig. 5**a**, compared with pure ZTL, the luminous intensity of ZTL/MT20% decreases and it show dramatically decrease in ZTL/Fe@MT20%, which suggests that the separation of the electrons and holes is enhanced by interfacing ZTL with Fe doped MT [54-56]. In addition, the transient photocurrent response of ZTL, ZTL/MT20% and ZTL/Fe@MT20% were employed to study the optical and photoelectrochemical properties. As shown in Fig. 5**b**, compared with ZTL, the enhanced photocurrent density can be observed in the composite

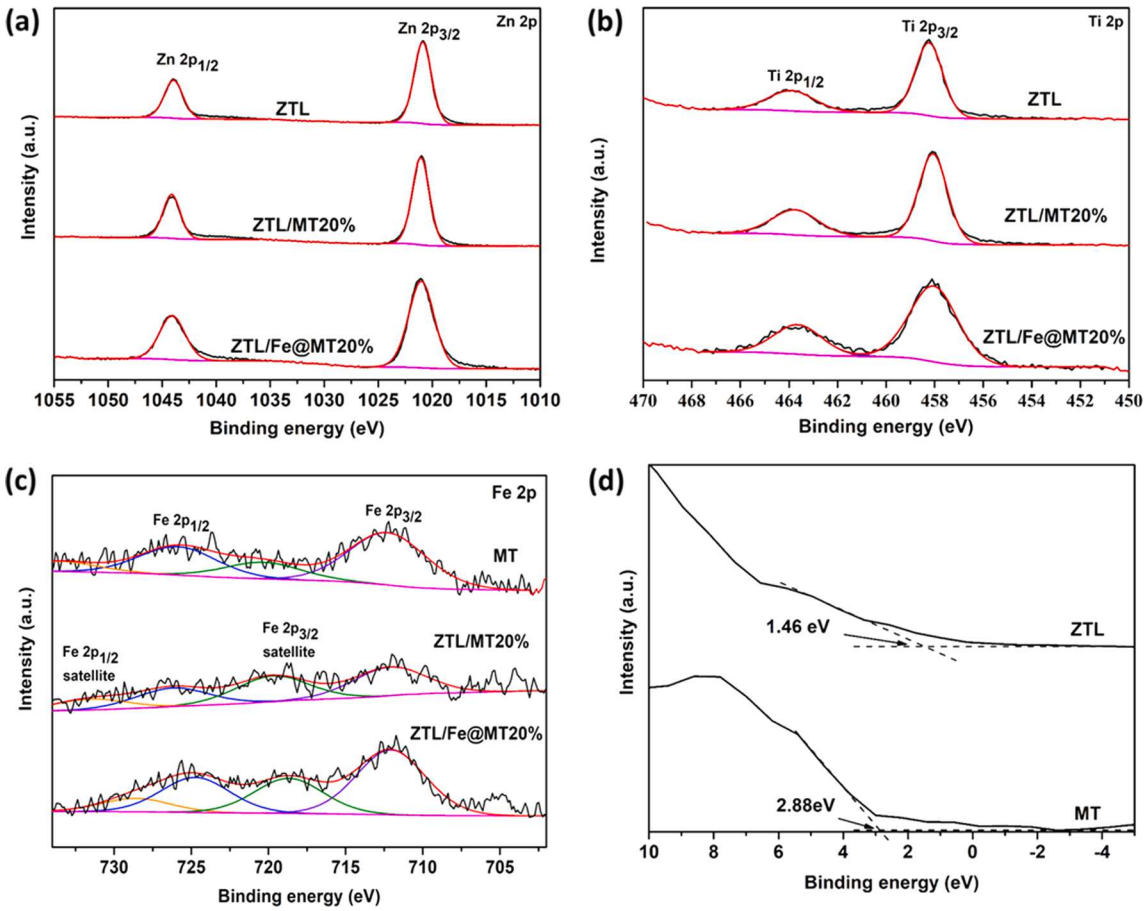

Fig. 3. XPS spectra of MT, ZTL, ZTL/MT20% and ZTL/Fe@MT20%: (a) Zn 2p, (b) Ti 2p, (c) Fe 2p and (d) valence band energy region of ZTL and MT.

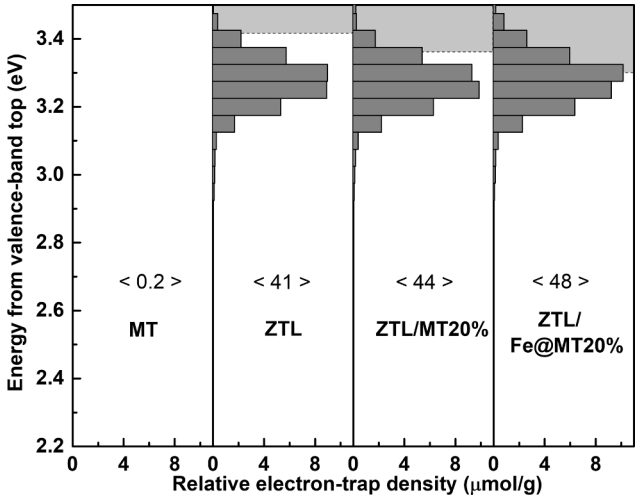

Fig. 4. Representative energy-resolved distribution of electron traps (ERDTs)/conduction band bottom (CBB) patterns of a series of MT, ZTL, ZTL/MT20% and ZTL/Fe@MT20% plotted as a function of energy (eV) from the valence band top (VBT) combined with CBB. The numbers in brackets denote the relative total electron-trap density.

samples. The ZTL/Fe@MT20% show the highest photocurrent density, suggesting that the heterojunction between ZTL and Fe doped on MT promoted photon to current conversion efficiency, which is in good agreement with the lowest recombination of electron and hole by PL results.

3.2. Photocatalytic reduction of Cr(VI)

To evaluate the photocatalytic activity of ZTL, ZTL/MT composites and ZTL/Fe@MT20%, the prepared samples was used as a photocatalyst for the photocatalytic reduction of Cr(VI) as shown in Fig. 6**a**. The pristine MT showed a negligible decrease in the Cr(VI) concentration under illumination, while the ZTL exhibited a strong activity toward Cr (VI). The result suggests that pure ZTL can be used as photocatalyst for Cr(VI) reduction, surpassing the performance of ZnO and TiO_2 [16]. Moreover, the ZTL/MT10% and ZTL/MT20% exhibited higher photocatalytic reduction of Cr(VI) compared with pure ZTL. The improvement of the photocatalytic efficiency of the composites can be attributed to the significant suppression of electron-hole recombination at the interface. The higher photocatalytic efficiency of ZTL/MT20% than ZTL/MT10% may due to higher contract area between MT and ZTL, which can enhance the separation of the electron-hole pairs. However, the photocatalytic reduction performance was seen to decrease for MT content above 20%, which might be less amount of ZTL main photocatalyst. The highest Cr(VI) photocatalytic reduction efficiency was obtained by ZTL/Fe@MT20% which has more Fe in the structure of MT compare with ZTL/MT20% and the reduction efficiency was further improved by addition the ethanol as a hole scavenger into the reaction (ZTL/Fe@MT20%-E) to enhance the separation of photogenerated charge carriers.

Fig. 6**b** displays the kinetics plot of the photocatalytic reduction of Cr (VI) over samples under light irradiation. The results of the photocatalytic reduction of Cr(VI) are in close agreement with a first-order kinetics model, enabling for the determination of the rate constants of each sample. Drawing on these results, it is clear that the rate constants of ZTL/Fe@MT20% are higher than those of the other composites,

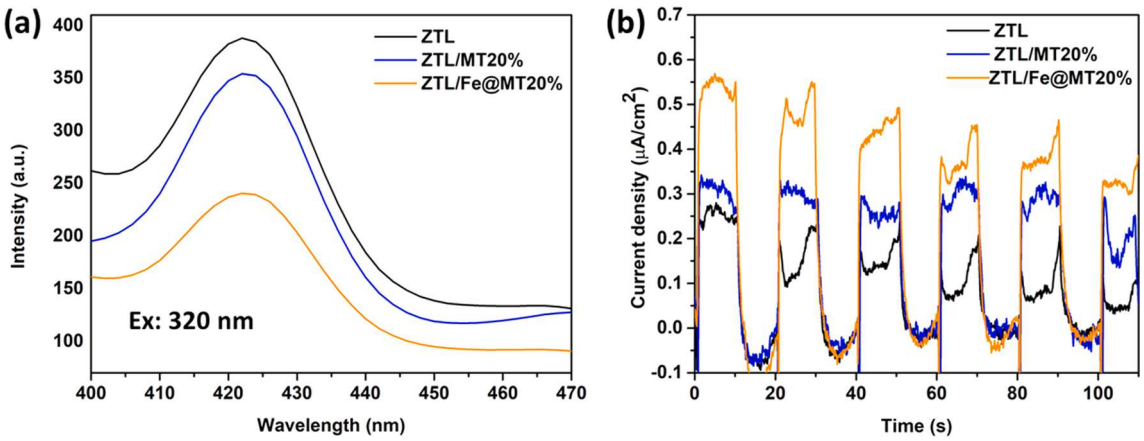

Fig. 5. (a) Photoluminescence spectra and (b) photocurrent of ZTL, ZTL/MT20% and ZTL/Fe@MT20%.

which is consistent with the lower efficiency observed in Fig. 6**a**. From the above results, the essential factor that leads to the improved photocatalytic reduction of Cr(VI) at ZTL/Fe doped MT heterojunctions is presumably the decreased recombination rate of the photogenerated charge carriers. Compared with other studies in different reaction systems (**Table S2**), the ZTL/Fe@MT20% show higher reduction efficiency in short time reaction than Fe_3O_4-ZnAl-layered double hydroxide/TiO_2, AgBr@Ag/CoAl LDH, PANI@C_3N_4/$ZnFe_2O_4$ and ZnO/$ZnAl_2O_4$ systems [57–60]. Also, the reduction efficiency of Cr(VI) by ZTL/Fe@MT20% could be comparable to a system of ZnO nanorods immobilized on kaolin at higher pH [61].

The effect of pH for photocatalytic Cr(VI) reduction over ZTL/Fe@MT20% was studied and results were shown in Fig. 6**c**. It was clear that the reduction activity decreased when pH increased and the pH 3 showed the best performance for Cr(VI) reduction than other pH condition. The high photocatalytic activity at low pH condition might be resulted from the higher positive reaction of rate constant in **Eq. (2)** to promote the production of Cr(III). However, when the pH of the reaction decreases to 2, the photocatalytic activity drops to around 53% because of the distortion of Zn-Ti LDH in the high acidic condition, confirmed by the disappear of the LDH phase in the XRD pattern of a spent-ZTL/Fe@MT20% at pH 2 as shown in Fig. 7. Also, in the high pH conditions, $Cr(OH)_3$ could be formed on the surface of the photocatalyst, resulting to decreasing of active surface of photocatalyst [62].

$$HCrO_4^- + 7H^+ + 3e^- \rightleftharpoons Cr^{3+} + 4H_2O \quad (2)$$

One of the critical factors determining the practical usability of a photocatalytic material is its chemical stability. The stability of ZTL/Fe@MT20% during Cr(VI) reduction was studied by five successive recycling tests. As shown in Fig. 6**d**, **a** slight decrease in the photocatalytic reduction of Cr(VI) was observed for ZTL/Fe@MT20%, possibly indicating that the Cr ion adsorb or precipitate on the surface of catalyst, some part of ZTL transforms under acid conditions and loss of some catalyst for next cycle.

The effect of catalyst loading was further studied and results were displayed in Fig. 6**e**. In the presence of light, the concentration of Cr(VI) was reduced with the increasing of ZTL/Fe@MT20% from 0.5 to 1.5 g/L due to the high production of electrons on the surface of the photocatalyst. However, the decreasing of the photocatalytic efficiency decrease with the further increasing of catalyst loading to 2.0 g/L because the solution became more turbid, leading to hindered penetration of light. The decreasing of the photocatalytic reduction of Cr(VI) can be observed with the reduction of the light power. From **Fig. S3**, when light power reduces from 25 W to 15 W, the Cr(VI) reduction efficiency decrease around 50% due to less photon energy. Moreover, the effect of reaction temperature was also investigated as shown in Fig. 6**f**. It can be seen that the reaction temperatures did not affect the photocatalytic reduction of Cr(VI).

To confirm the stability of ZTL after the photocatalytic reaction, the spent ZTL/Fe@MT20% at different pH conditions was collected after 1 cycle of the photocatalytic Cr(VI) reduction. As illustrated in Fig. 7, the main diffraction peak of ZTL still remains in the XRD pattern of the spent ZTL/MT20% and spent ZTL/Fe@MT20%, indicating that the ZTL structure is maintained upon photocatalytic reduction of Cr(VI). Moreover, the interlayer peak of MT in spent ZTL/MT20% was shifted to a lower diffraction angle (from 7.3° to 6.0° 2θ) corresponding to an expansion of interlayer spacing in MT (from 12.48 Å to 14.57 Å). Based on previous reports, it is well establish that MT is an excellent cationic exchanger from aqueous solution [63,64]. Thus, the produced Cr(III) species after photocatalytic reduction of Cr(VI) are likely to be intercalated between the layer of MT by cationic exchange with Na^+ in MT, thus expanding the interlayer spacing in MT due to the increased ionic size and electrostatic interactions of Cr^{3+} relative to Na^+ [65]. However, the spent ZTL/Fe@MT20% showed the shifting of interlayer peak of MT in to higher diffraction angle compare with fresh ZTL/Fe@MT20% and the peak has more shift when the pH of reaction increase, implying to be the releasing of intercalated Fe from the interlayer of MT during the reaction, according to decreasing of photocatalytic reusability.

The chemical state of the elements in spent ZTL/Fe@MT20% was also investigated by means of XPS. Fig. 8 display the spectrum of Zn, Ti and Fe of ZTL/Fe@MT20% and spent ZTL/Fe@MT20%. The binding energy E_B[Zn $2p_{3/2}$] = 1021.5 eV for the spent ZTL/Fe@MT20% indicates that the chemical state of Zn does not change even after the reduction of Cr(VI) (Fig. 8**a**). Similarly, Fig. 8**b and 8c** show peaks at E_B[Ti $2p_{3/2}$] = 458.3 eV and E_B[Fe $2p_{3/2}$] = 712.9 eV, confirming the absence of chemical reduction of Ti and Fe. The chemical state of Zn, Ti and Fe do not change even after the reaction, suggesting the stability of ZTL/Fe@MT20% under photocatalytic reduction of Cr(VI. Furthermore, Examining the XPS Cr 2p spectrum (Fig. 8**d**), a peak at E_B[Cr $2p_{3/2}$] = 576.8 eV, which is assigned to Cr(III) and confirms the photoreduction of Cr(VI) , resulting that there may exist some Cr^{3+} adsorb on the surface and/or intercalated between the layer of MT in ZTL/Fe@MT20%.

The distribution of Cr in ZTL/Fe@MT20% was confirmed by TEM-EDX for the spent photocatalyst. Fig. 9 shows some Ti-containing particles are formed, which are plausibly derived from the conversion of ZTL into titanium oxide. Moreover, the distribution of Cr in spent catalyst overlap with in the MT and Ti location, overlapping with Si, Mg, Al and Ti, confirming that the existing of the produced Cr(III) might be intercalated and/or precipitated between the MT layers, thereby further shifting the photo-electrochemical equilibrium. The strong overlap of Cr in the location of Ti might be due to adsorption of Cr ion on the surface of TiO_2 [62],[66–68].

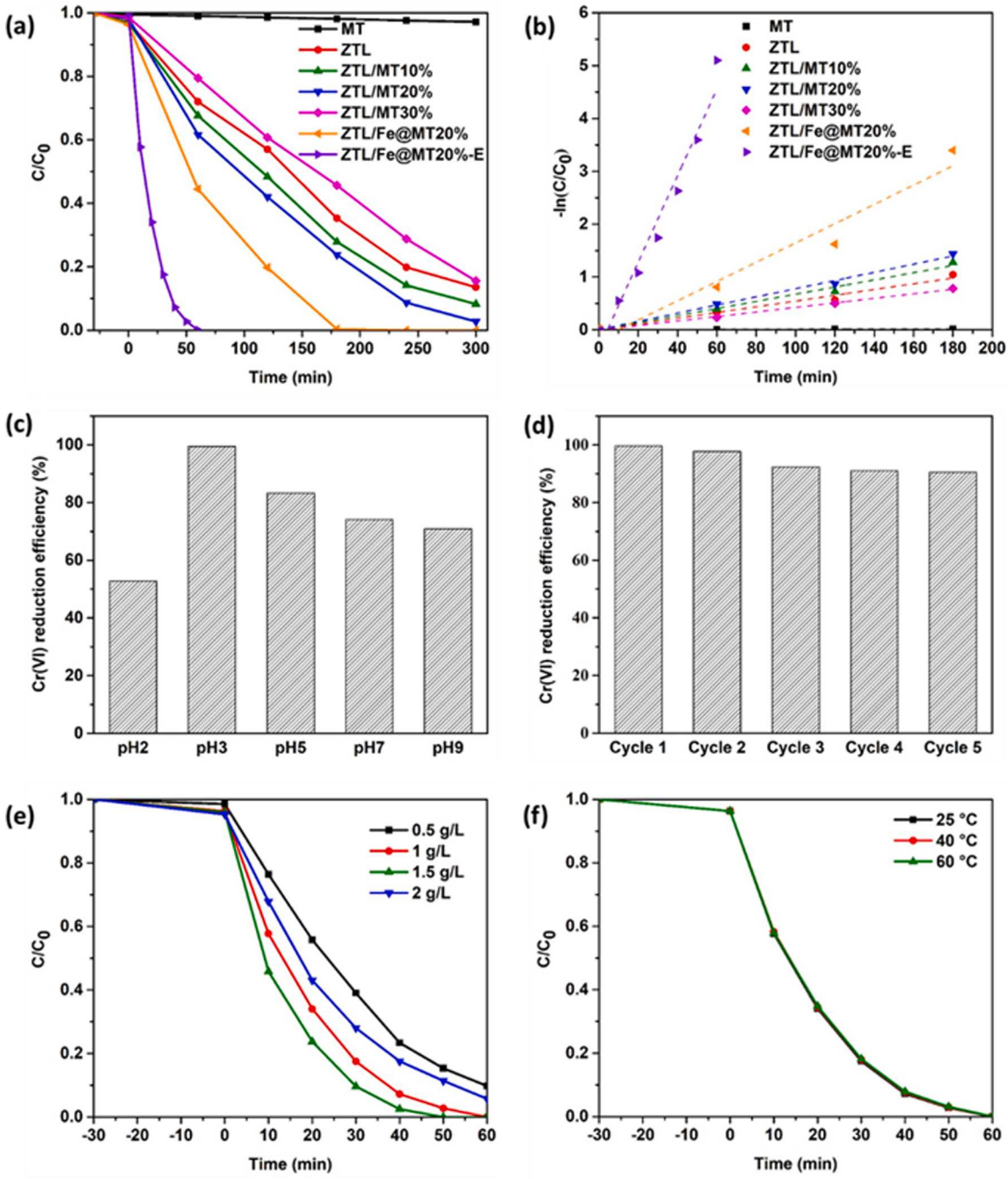

Fig. 6. (a) Photocatalytic reduction of Cr(VI) with time, (b) kinetic linear fitting curves of MT, ZTL, ZTL/MT composites and ZTL/Fe@MT20%, (c) effect of pH on the reduction of Cr(VI), (d) recycling test, (e) effect of catalyst loading on the reduction of Cr(VI) and (f) effect of temperature on the reduction of Cr(VI).

3.3. Photocatalytic mechanism of Cr(VI) reduction

It is known that interfacial charge separation can increase the photocurrent, thus enhancing the photocatalytic reduction activity. As discussed in the previous sections, the composites showed higher photocatalytic performance than each individual ZTL and MT. Also, the activity dramatically increased in high content of Fe sample (ZTL/Fe@MT20%), which suggests that the Fe impurity in MT might play important role for prevent the charge recombination through the heterojunction. To understand the underlying charge transfer mechanisms, first-principles calculations were performed to calculate the density of states (DOS) of both ZTL and Fe-bearing MT, as shown in Fig. 10.

For these calculations, we constructed a model Fe-bearing MT structure derived from the chemical formula $NaSi_8Al_4O_{20}(OH)_4{\cdot}4H_2O$ in the dioctahedral geometry [69]. To account for Fe impurities, one of the Al atoms within the tetrahedra-octahedra-tetrahedra framework is substituted with Fe. The model ZTL structure is constructed following Costa et al. [70], with CO_3^{2-} inserted between the layers.

By carrying out a full geometry optimization of the Fe-bearing MT and ZTL unit cells, we obtained the electronic density of states shown in Fig. 10**a and b**, where it is clearly seen that the introduction of Fe creates mid-gap electronic states and that these defect levels are mainly contributed by the Fe *d* orbitals. Specifically, the optical response of Fe-bearing MT is determined by excitations from the valence band edge (mainly related to the O orbitals) to the conduction band edge (mainly related to the Fe orbitals), corresponding to an optical energy threshold of 5.16 eV. For ZTL, the calculated band gap is of 2.81 eV, which is in good agreement with the experimental measurement, albeit slightly

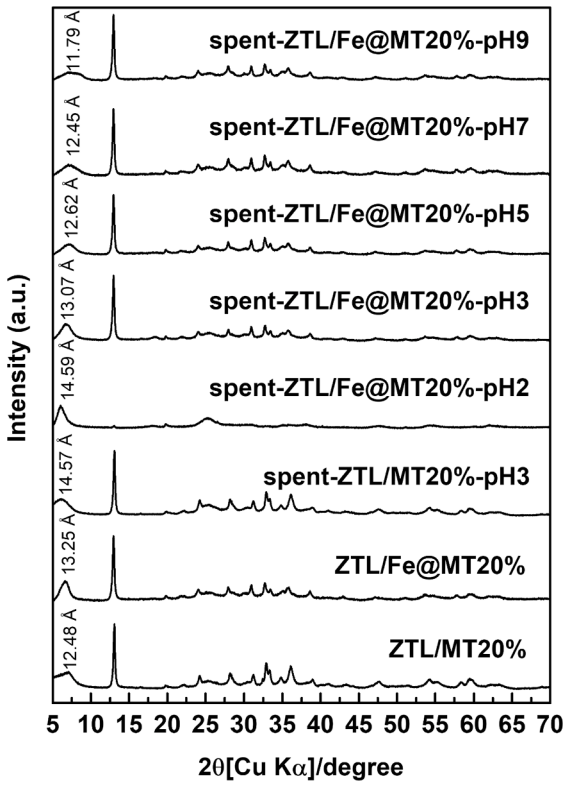

Fig. 7. XRD patterns of the fresh and spent ZTL/MT20% and ZTL/Fe@MT20%.

underestimated.

To evaluate the band edges, slabs of Fe-bearing MT and ZTL are constructed along the [0 0 1] direction with a vacuum separation of 15 Å. In addition, solvation effects are taken into account by immersing the interface into a polarizable continuum using the self-consistent continuum solvation method (SCCS) [71]. The relaxed interface structures for both ZTL and Fe-bearing MT are show in Fig. 11.

To evaluate the stability of these surfaces in aqueous environments under experimentally relevant conditions (pH 3), we calculated the adsorption energy of a proton at the Fe-bearing MT-water and ZTL-water interfaces; the free energy of adsorption is calculated as

$$\Delta G_H = \Delta F_H + \Delta ZPE_H - T\Delta S_H \tag{3}$$

$$\Delta F_H = E_{H^*} - E_* - \frac{1}{2}E_{H_2(g)} - K_b T ln(10) pH \tag{4}$$

$$\Delta ZPE_H = ZPE_{H^*} - \frac{1}{2}\Delta ZPE_{H_2(g)} \tag{5}$$

where ΔF_H is the energy change upon adsorption, E_{H^*}, E_* and $E_{H_2(g)}$ are the energies of the interface with adsorbed hydrogen, of the pristine interface and of molecular hydrogen, respectively. Additionally, ΔF_H includes the free energy change of the proton at finite pH. The ΔZPE_H and ΔS_H are the change in zero-point vibrational energy and entropy upon adsorption. The zero-point energy of the adsorbed protons is calculated at the Γ-point. The entropy corrections of the reference hydrogen gas are taken from experimental measurements [72]. The free energies ΔG_H of proton adsorption at the two symmetrically unique sites of the Fe-bearing MT surface are calculated to be 5.06 eV and 4.99 eV, which indicates that the protons are unstable at the Fe-bearing MT-water interface at pH 3. In contrast, the free energy of proton adsorption

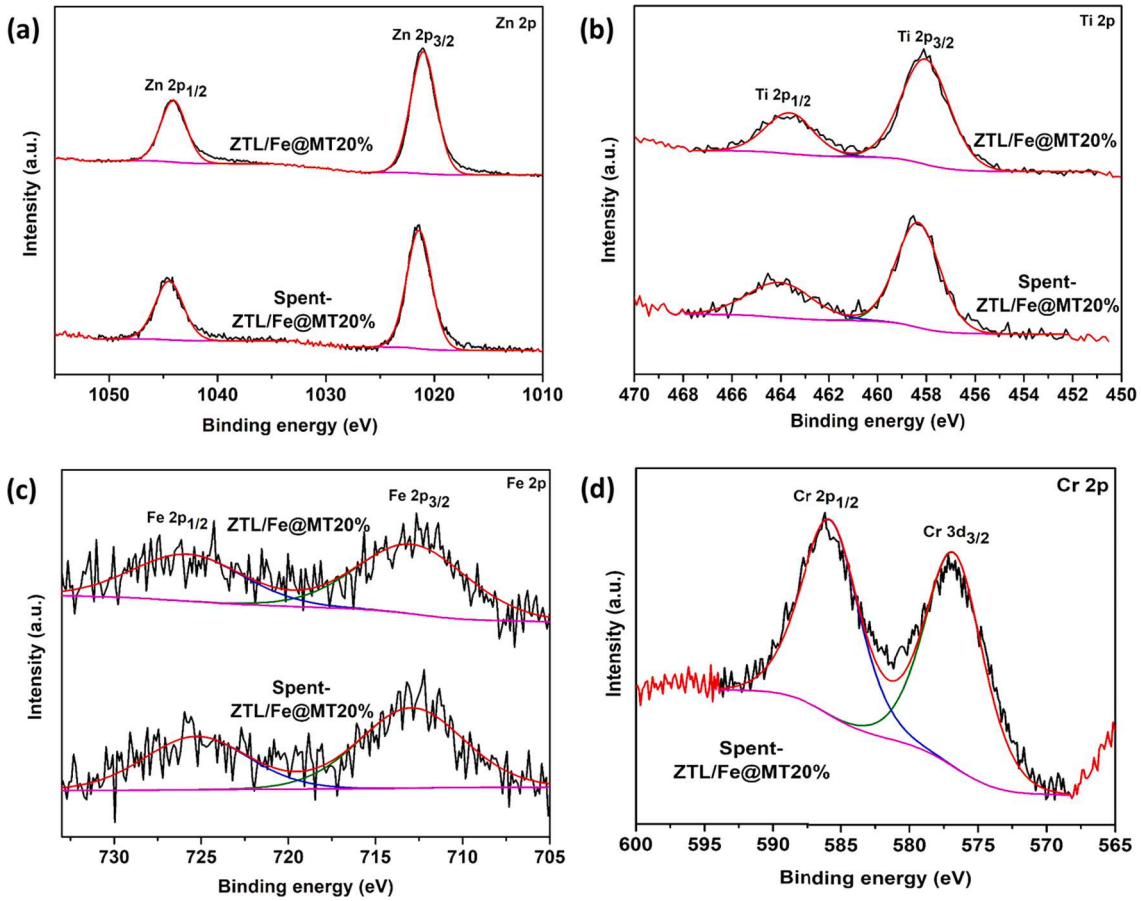

Fig. 8. XPS spectra for the fresh and spent ZTL/MT20% and ZTL/Fe@MT20%: (a) Zn 2p, (b) Ti 2p, (c) Fe 2p and (d) Cr 2p.

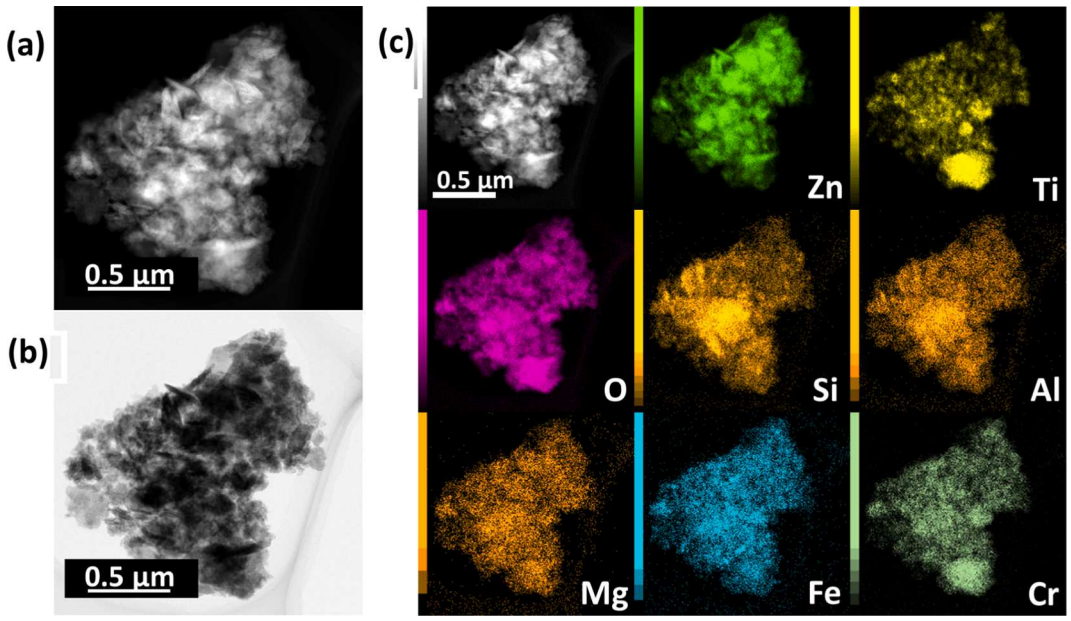

Fig. 9. TEM-EDX elemental mapping of Zn, Ti, Si, O, Al, Mg, Fe and Cr in spent ZTL/Fe@MT20%.

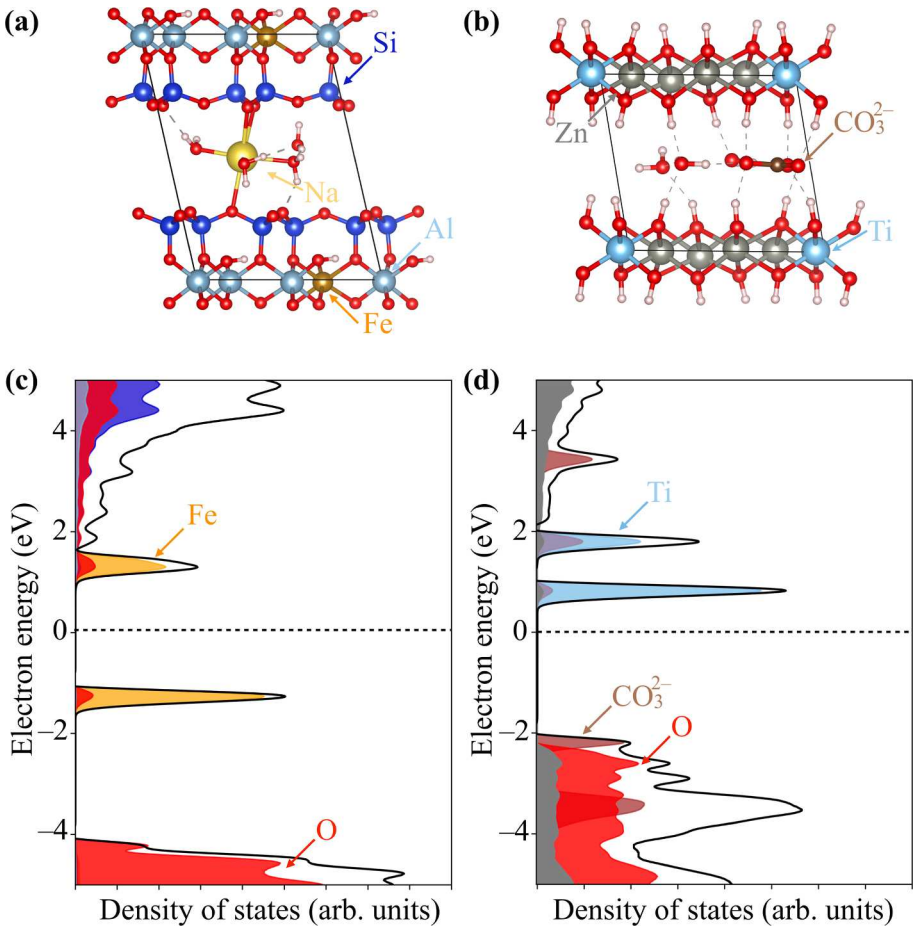

Fig. 10. Optimized structures of (a) Fe-bearing MT and (b) ZTL. The projected density of states of Fe-bearing MT and ZTL are shown in panels (c) and (d), respectively.

at the Ti-O site of the ZTL-water interface is of –1.17 eV, whereas it is calculated to be of 0.23 eV at the Zn-O site.

Using the calculated stable surface structures, we evaluate the band edge positions from the calculated Fermi level relative to the reference electrostatic energy of the solvation continuum, yielding the positions of conduction band (E_c) and valence band (E_v):

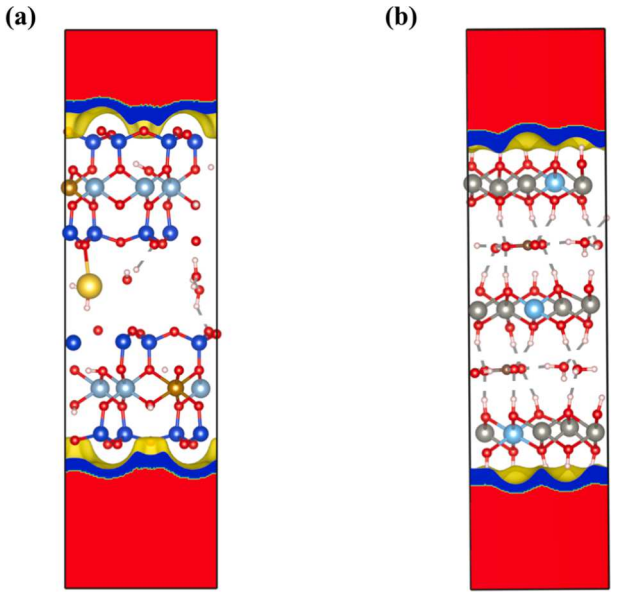

Fig. 11. Surface structures of (a) Fe-bearing MT and (b) ZTL that are relaxed in the implicit solvent. The colored regions represent the aqueous environment.

$$E_c = E_f + 0.5E_g \quad (6)$$

$$E_v = E_f - 0.5E_g \quad (7)$$

where E_g denotes the band gap. The resulting band alignment of Fe-bearing MT and ZTL with respect to the potentials of the redox couples are calculated from Eqs. (6) and (7). The calculated VB and CB positions of ZTL are of 1.46 and –1.36 V, respectively, while the band gap and VB of Fe-bearing MT are found to be of approximately 3.88 eV and –1.28 V, respectively. Moreover, the mid-gap state position of Fe on MT is estimated to be of 1.09 V from the band alignment of Fe-bearing MT, using the calculated stable surface structures.

Generally, a transfer of photogenerated charge carriers through the interfacial contract of a matched energy band structure is the important factor to prolong the lifetime of the charge carriers, resulting in enhancing the photocatalytic activity. From PL and photocurrent response results, the composites show lower recombination of electron and hole than pure ZTL, suggesting that the heterojunction between ZTL and MT can avoid the electron-hole recombination. Based on the calculated band edges, two possible types of heterojunctions, conventional-type II heterojunction and Z-scheme heterojunction, could be formed between ZTL and MT. To consider the reduction of Cr(VI), the necessary electrons in an appropriate energy level are required to reduce dissolved Cr(VI) in solution. However, the position of the mid-gap state of Fe on MT, which is an electron acceptor level was more negative than the standard potential of reduction of Cr(VI)/Cr(III) (0.96 V), indicating that the photogenerated electrons in this state could not reduce Cr(VI) into Cr(III). Moreover, the negative surface charge of MT will disfavor the adsorption of $HCrO_4^-$ anions due to electrostatic repulsion, which might decrease the photocatalytic efficiency because of less interaction of the $HCrO_4^-$ anions and photocatalyst. The photocatalytic Cr(VI) reduction activity would not be improved if the photogenerated electrons were transferred through the type II heterojunction. Thus, a Z-scheme photocatalytic mechanism of charge transfers in the composites was proposed, based on the characteristic of transfers of photogenerated electrons from high electronic state to low electronic state, as shown in Scheme 1. Upon irradiation, the ZTL can absorb photons and then produce photogenerated electron in the CB (-1.36 V) and photogenerated holes in VB (1.46 V), while the electrons from the VB of Fe-bearing MT (3.88 V) are excited to the Fe-mid-gap states of MT (1.09 V). The photogenerated electrons in this mid-gap state (1.09 V) can transfer to the

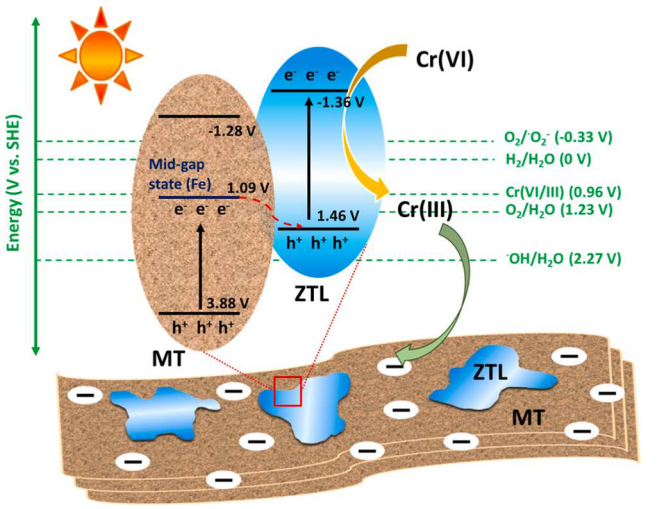

Scheme 1. The band edge positions of Fe-bearing MT and ZTL with respect to standard hydrogen electrode (SHE), where the $E_{(\text{vs SHE})} = -(E_{(\text{vs vacuum})} - 4.44)$ V. The middle-gap states in MT is at 1.09 V/SHE.

VB of ZTL due to the more positive energy of the VB of ZTL (1.46 V) relative to the VB state of MT (3.88 V). The recombination of electrons from Fe-mid-gap states of MT and holes in VB of ZTL can promote the separation of photogenerated charge carrier of ZTL and maintain the electron in the CB of ZTL. Thus, the superior photocatalytic performance the ZTL/MT composites and ZTL/Fe@MT20% might be come from the Z-scheme ZTL/MT heterojunction, which suppresses electron-hole recombination. For photocatalytic reduction of Cr(VI), the dissolved Cr(VI) in the solution can react with an electron in CB of ZTL to convert into Cr(III). Furthermore, the produced Cr(III) might be adsorbed and/or intercalated between MT layers, which can decrease the mobility of toxic Cr(III) ions into the solid phase. From the above discussion, the photocatalytic reduction of Cr(VI) could be described as the following sequence of equation:

$$\text{ZTL/MT} + h\nu \rightarrow \text{ZTL}(h^+ + e^-)/\text{MT}\ (h^+ + e^-) \quad (8)$$

$$\text{ZTL}(h^+)/\text{MT}\ (e^-) \rightarrow \text{ZTL/MT} \quad (9)$$

$$HCrO_4^- + 7H^+ + \text{ZTL}(3e^-) \rightarrow Cr^{3+} + 4H_2O + \text{ZTL} \quad (10)$$

$$\text{ZTL}(h^+)/\text{MT} + 2H_2O + 4\ h^+ \rightarrow \text{ZTL/MT} \quad (11)$$

4. Conclusions

ZTL/MT and ZTL/Fe@MT20% composites were successfully prepared, and the photocatalytic activity of these composites toward Cr(VI) reduction was systematically characterized using a range of complementary experimental method. The ZTL/Fe@MT20% composite exhibited the highest reduction efficiency and kinetic rate for photocatalytic reduction of Cr(VI), due to efficient light absorption and low electron-hole recombination rates. Interestingly, DFT calculations suggest that electron promotion into the mid-gap state of MT, arising from Fe impurities, is followed by electron transfer to the VB of ZTL, thereby enhancing charge separation in ZTL and increasing the photocatalytic activity. Moreover, Fe-containg MT in the ZTL/MT and ZTL/Fe@MT20% not only provide substantial suppression of charge recombination but also offer an effective pathway to accumulate Cr(III) on the surface and/or within the interlayer spacing of MT, thus shifting the overall photo-electrochemical equilibrium. This finding demonstrates the promising practical potential of a wide range of clay minerals for cost-effective, sunlight-driven environmental remediation.

CRediT authorship contribution statement

Chitiphon Chuaicham: Conceptualization, Investigation, Formal analysis, Writing - original draft, Writing - review & editing. **Yihuang Xiong:** Formal analysis. **Karthikeyan Sekar:** Formal analysis. **Weinan Chen:** Formal analysis. **Li Zhang:** Formal analysis. **Bunsho Ohtani:** Investigation. **Ismaila Dabo:** Investigation. **Keiko Sasaki:** Conceptualization, Investigation, Writing - review & editing.

Declaration of Competing Interest

The authors declare that they have no known competing financial interests or personal relationships that could have appeared to influence the work reported in this paper.

Acknowledgements

The authors acknowledge financial supports from Japan Society for the Promotion of Science (JSPS) KAKENHI (A) (No. JP18F18387), Cooperative Research Programs at Hokkaido University Institute for Catalysis (Nos. 18A1001, 19B1002 and 20A1001) and Kyushu University (Progress 100) to KS and the National Science Foundation (NSF) under grant number DMREF-1729338 to ID. XPS measurements were carried out in Nanotech Center, Kyushu University and TEM-EDX images were observed in HVEM Center, Kyushu University. The computational work was performed using high-performance computing resources from the Penn State Institute of Cyberscience.

Appendix A. Supplementary material

Supplementary data to this article can be found online at https://doi.org/10.1016/j.apsusc.2020.148835.

References

[1] M. Shirzad-Siboni, M. Farrokhi, R.D.C. Soltani, A. Khataee, S. Tajassosi, Photocatalytic reduction of hexavalent chromium over ZnO nanorods immobilized on kaolin, Ind. Eng. Chem. Res. 53 (2014) 1079–1087.
[2] A. Mohamed, T.A. Osman, M.S. Toprak, M. Muhammed, E. Yilmaz, A. Uheida, Visible light photocatalytic reduction of Cr(VI) by surface modified CNT/titanium dioxide composites nanofibers, J Mol Catal a-Chem 424 (2016) 45–53.
[3] F.C. Richard, A.C.M. Bourg, Aqueous geochemistry of chromium – a review, Water Res. 25 (1991) 807–816.
[4] S.H. Kang, G.Z. Wang, H.J. Zhaoa, W.P. Cai, Highly efficient removal of hexavalent chromium in aqueous solutions via chemical reduction of plate-like micro/nanostructured zero valent iron, RSC Adv. 7 (2017) 55905–55911.
[5] P. Lakshmipathiraj, G.B. Raju, M.R. Basariya, S. Parvathy, S. Prabhakar, Removal of Cr (VI) by electrochemical reduction, Sep. Purif. Technol. 60 (2008) 96–102.
[6] A. Demir, M. Arisoy, Biological and chemical removal of Cr(VI) from waste water: cost and benefit analysis, J Hazard Mater 147 (2007) 275–280.
[7] A. Hafiane, D. Lemordant, M. Dhahbi, Removal of hexavalent chromium by nanofiltration, Desalination 130 (2000) 305–312.
[8] F. Xu, H. Chen, C. Xu, D. Wu, Z. Gao, Q. Zhang, K. Jiang, Ultra-thin Bi2WO6 porous nanosheets with high lattice coherence for enhanced performance for photocatalytic reduction of Cr(VI), J. Colloid Interface Sci. 525 (2018) 97–106.
[9] Z. Lv, H. Zhou, H. Liu, B. Liu, M. Liang, H. Guo, Controlled assemble of oxygen vacant CeO2@Bi2WO6 hollow magnetic microcapsule heterostructures for visible-light photocatalytic activity, Chem. Eng. J. 330 (2017) 1297–1305.
[10] D.K. Padhi, T.K. Panigrahi, K. Parida, S.K. Singh, P.M. Mishra, Green synthesis of Fe3O4/RGO nanocomposite with enhanced photocatalytic performance for Cr(VI) reduction, phenol degradation, and antibacterial activity, ACS Sustain. Chem. Eng. 5 (2017) 10551–10562.
[11] G. Zhang, D. Chen, N. Li, Q. Xu, H. Li, J. He, J. Lu, SnS2/SnO2 heterostructured nanosheet arrays grown on carbon cloth for efficient photocatalytic reduction of Cr (VI), J. Colloid Interface Sci. 514 (2018) 306–315.
[12] E. Park, Y. Lee, V.D. Dao, N.T.D. Cam, H.S. Choi, Design of CoNi alloy/graphene as an efficient Pt-free counter electrode in liquid junction photovoltaic devices, Synth. Met. 230 (2017) 97–104.
[13] H. Wei, Y. Wen, Y. Zhang, Nitric acid-assisted one-step solvothermal synthesis of visible-light-active N-doped ThO2 for use as a potential photocatalyst in the reduction of Cr(VI), Catal. Commun. 99 (2017) 66–70.
[14] S. Mansingh, D.K. Padhi, K.M. Parida, Enhanced visible light harnessing and oxygen vacancy promoted N, S co-doped CeO2 nanoparticle: a challenging photocatalyst for Cr(vi) reduction, Catal. Sci. Technol. 7 (2017) 2772–2781.
[15] X. Meng, G. Zhang, N. Li, Bi24Ga2O39 for visible light photocatalytic reduction of Cr(VI): Controlled synthesis, facet-dependent activity and DFT study, Chem. Eng. J. 314 (2017) 249–256.
[16] Y. Deng, L. Tang, G. Zeng, Z. Zhu, M. Yan, Y. Zhou, J. Wang, Y. Liu, J. Wang, Insight into highly efficient simultaneous photocatalytic removal of Cr(VI) and 2,4-diclorophenol under visible light irradiation by phosphorus doped porous ultrathin g-C3N4 nanosheets from aqueous media: Performance and reaction mechanism, Appl. Catal. B 203 (2017) 343–354.
[17] Y. Shi, X. Xiong, S. Ding, X. Liu, Q. Jiang, J. Hu, In-situ topotactic synthesis and photocatalytic activity of plate-like BiOCl/2D networks Bi2S3 heterostructures, Appl. Catal. B 220 (2018) 570–580.
[18] G. Velegraki, J. Miao, C. Drivas, B. Liu, S. Kennou, G.S. Armatas, Fabrication of 3D mesoporous networks of assembled CoO nanoparticles for efficient photocatalytic reduction of aqueous Cr(VI), Appl. Catal. B 221 (2018) 635–644.
[19] K. Li, Y. Liang, J. Yang, H. Zhang, G. Yang, W. Lei, BiOCl/Fe2O3 heterojunction nanoplates with enhanced visible-light-driven photocatalytic performance for degrading organic pollutants and reducing Cr(VI), J. Photochem. Photobiol., A 364 (2018) 240–249.
[20] Z. Fan, Y. Zhao, W. Zhai, L. Qiu, H. Li, M.R. Hoffmann, Facet-dependent performance of BiOBr for photocatalytic reduction of Cr(vi), RSC Adv. 6 (2016) 2028–2031.
[21] J. Jiang, Z. Mu, P. Zhao, H. Wang, Y. Lin, Photogenerated charge behavior of BiOI/g-C3N4 photocatalyst in photoreduction of Cr (VI): A novel understanding for high-performance, Mater. Chem. Phys. 252 (2020), 123194.
[22] C. Alanis, R. Natividad, C. Barrera-Diaz, V. Martínez-Miranda, J. Prince, J. S. Valente, Photocatalytically enhanced Cr(VI) removal by mixed oxides derived from MeAl (Me: Mg and/or Zn) layered double hydroxides, Appl. Catal. B 140–141 (2013) 546–551.
[23] Y.F. Zhao, X.D. Jia, G.I.N. Waterhouse, L.Z. Wu, C.H. Tung, D. O'Hare, T.R. Zhang, Layered double hydroxide nanostructured photocatalysts for renewable energy production, Adv. Energy Mater. 6 (2016) 1501974.
[24] C. Gomes Silva, Y. Bouizi, V. Fornes, H. Garcia, Layered double hydroxides as highly efficient photocatalysts for visible light oxygen generation from water, J. Am. Chem. Soc. 131 (2009) 13833–13839.
[25] M.J. Wu, J.Z. Wu, J. Zhang, H. Chen, J.Z. Zhou, G.R. Qian, Z.P. Xu, Z. Du, Q.L. Rao, A review on fabricating heterostructures from layered double hydroxides for enhanced photocatalytic activities, Catal. Sci. Technol. 8 (2018) 1207–1228.
[26] C.M. Puscasu, E.M. Seftel, M. Mertens, P. Cool, G. Carja, ZnTiLDH and the derived mixed oxides as mesoporous nanoarchitectonics with photocatalytic capabilities, J. Inorg. Organomet. Polym Mater. 25 (2015) 259–266.
[27] Y.P. Zhu, R.L. Zhu, G.Q. Zhu, M.M. Wang, Y.N. Chen, J.X. Zhu, Y.F. Xi, H.P. He, Plasmonic Ag coated Zn/Ti-LDH with excellent photocatalytic activity, Appl. Surf. Sci. 433 (2018) 458–467.
[28] S.-J. Xia, F.-X. Liu, Z.-M. Ni, J.-L. Xue, P.-P. Qian, Layered double hydroxides as efficient photocatalysts for visible-light degradation of Rhodamine B, J. Colloid Interface Sci. 405 (2013) 195–200.
[29] S.-J. Xia, F.-X. Liu, Z.-M. Ni, W. Shi, J.-L. Xue, P.-P. Qian, Ti-based layered double hydroxides: Efficient photocatalysts for azo dyes degradation under visible light, Appl. Catal. B 144 (2014) 570–579.
[30] M. Shao, J. Han, M. Wei, D.G. Evans, X. Duan, The synthesis of hierarchical Zn–Ti layered double hydroxide for efficient visible-light photocatalysis, Chem. Eng. J. 168 (2011) 519–524.
[31] Y. Zhu, M. Laipan, R. Zhu, T. Xu, J. Liu, J. Zhu, Y. Xi, G. Zhu, H. He, Enhanced photocatalytic activity of Zn/Ti-LDH via hybridizing with C60, Molecular Catalysis 427 (2017) 54–61.
[32] N. Tian, Y. Zhang, C. Liu, S. Yu, M. Li, H. Huang, g-C3N4/Bi4O5I2 2D–2D heterojunctional nanosheets with enhanced visible-light photocatalytic activity, RSC Adv. 6 (2016) 10895–10903.
[33] Y.-J. Yuan, Z. Shen, S. Wu, Y. Su, L. Pei, Z. Ji, M. Ding, W. Bai, Y. Chen, Z.-T. Yu, Z. Zou, Liquid exfoliation of g-C3N4 nanosheets to construct 2D–2D MoS2/g-C3N4 photocatalyst for enhanced photocatalytic H2 production activity, Appl. Catal. B 246 (2019) 120–128.
[34] Y.-J. Yuan, D. Chen, J. Zhong, L.-X. Yang, J. Wang, M.-J. Liu, W.-G. Tu, Z.-T. Yu, Z.-G. Zou, Interface engineering of a noble-metal-free 2D–2D MoS2/Cu-ZnIn2S4 photocatalyst for enhanced photocatalytic H2 production, J. Mater. Chem. A 5 (2017) 15771–15779.
[35] S. Das, S. Patnaik, K.M. Parida, Fabrication of a Au-loaded CaFe2O4/CoAl LDH p–n junction based architecture with stoichiometric H2 & O2 generation and Cr(vi) reduction under visible light, Inorg. Chem. Front. 6 (2019) 94–109.
[36] X. Yuan, X. Cheng, Q. Jing, J. Niu, D. Peng, Z. Feng, X. Wu, ZnO/ZnAl(2)O(4) nanocomposite with 3D sphere-like hierarchical structure for photocatalytic reduction of aqueous Cr(VI), Materials 11 (2018) 1624.
[37] H. Li, X. Hao, Y. Liu, Y. Li, Z. Jin, ZnxCd1-xS nanoparticles dispersed on CoAl-layered double hydroxide in 2D heterostructure for enhanced photocatalytic hydrogen evolution, J. Colloid Interface Sci. 572 (2020) 62–73.
[38] C.Q. Li, Z.M. Sun, W.X. Huang, S.L. Zheng, Facile synthesis of g-C3N4/montmorillonite composite with enhanced visible light photodegradation of rhodamine B and tetracycline, J. Taiwan Inst. Chem. Eng. 66 (2016) 363–371.
[39] I. Fatimah, S.B. Wang, D. Wulandari, ZnO/montmorillonite for photocatalytic and photochemical degradation of methylene blue, Appl. Clay Sci. 53 (2011) 553–560.
[40] P.P. Li, L.Y. Huang, Y.P. Li, Y.G. Xu, S.Q. Huang, D. Yuan, H. Xu, H.M. Li, Synthesis of dark orange montmorillonite/g-C3N4 composites and their applications in the environment, J. Phys. Chem. Solids 107 (2017) 131–139.
[41] T. Hu, H. Li, N. Du, W. Hou, Iron-doped bismuth tungstate with an excellent photocatalytic performance, ChemCatChem 10 (2018) 3040–3048.

[42] T.-H. Xie, X. Sun, J. Lin, Enhanced photocatalytic degradation of RhB driven by visible light-induced MMCT of Ti(IV)−O−Fe(II) formed in Fe-doped SrTiO3, The Journal of Physical Chemistry C 112 (2008) 9753–9759.
[43] S.J. Kim, Y. Lee, D.K. Lee, J.W. Lee, J.K. Kang, Efficient Co–Fe layered double hydroxide photocatalysts for water oxidation under visible light, J. Mater. Chem. A 2 (2014) 4136–4139.
[44] W.H. Luo, K. Sasaki, T. Hirajima, Surfactant-modified montmorillonite by benzyloctadecyldimethylammonium chloride for removal of perchlorate, Colloid Surface A 481 (2015) 616–625.
[45] P. Giannozzi, S. Baroni, N. Bonini, M. Calandra, R. Car, C. Cavazzoni, D. Ceresoli, G.L. Chiarotti, M. Cococcioni, I. Dabo, A. Dal Corso, S. de Gironcoli, S. Fabris, G. Fratesi, R. Gebauer, U. Gerstmann, C. Gougoussis, A. Kokalj, M. Lazzeri, L. Martin-Samos, N. Marzari, F. Mauri, R. Mazzarello, S. Paolini, A. Pasquarello, L. Paulatto, C. Sbraccia, S. Scandolo, G. Sclauzero, A.P. Seitsonen, A. Smogunov, P. Umari, R.M. Wentzcovitch, QUANTUM ESPRESSO: a modular and open-source software project for quantum simulations of materials, Journal of physics, Condensed Matter: Institute of Physics J. 21 (2009), 395502.
[46] J.P. Perdew, Jacob's ladder of density functional approximations for the exchange-correlation energy, AIP Conf. Proc. 577 (2001) 1–20.
[47] N. Marzari, D. Vanderbilt, A. De Vita, M.C. Payne, Thermal contraction and disordering of the Al(110) surface, Phys. Rev. Lett. 82 (1999) 3296–3299.
[48] Z.A. Zakaria, Z. Zakaria, S. Surif, W.A. Ahmad, Hexavalent chromium reduction by Acinetobacter haemolyticus isolated from heavy-metal contaminated wastewater, J. Hazard Mater. 146 (2007) 30–38.
[49] G. Zhang, X. Zhang, Y. Meng, G. Pan, Z. Ni, S. Xia, Layered double hydroxides-based photocatalysts and visible-light driven photodegradation of organic pollutants: a review, Chem. Eng. J. 392 (2020), 123684.
[50] X.-J. Yang, B. Chen, X.-B. Li, L.-Q. Zheng, L.-Z. Wu, C.-H. Tung, Photocatalytic organic transformation by layered double hydroxides: highly efficient and selective oxidation of primary aromatic amines to their imines under ambient aerobic conditions, Chem. Commun. 50 (2014) 6664–6667.
[51] C. Chuaicham, R. Pawar, K. Sasaki, Dye-sensitized photocatalyst of sepiolite for organic dye degradation, Catalysts 9 (2019) 235.
[52] C. Chuaicham, S. Karthikeyan, R.R. Pawar, Y. Xiong, I. Dabo, B. Ohtani, Y. Kim, J. T. Song, T. Ishihara, K. Sasaki, Energy-resolved distribution of electron traps for O/S-doped carbon nitrides by reversed double-beam photoacoustic spectroscopy and the photocatalytic reduction of Cr(vi), Chem Commun (Camb) 56 (2020) 3793–3796.
[53] C. Chuaicham, S. Karthikeyan, J.T. Song, T. Ishihara, B. Ohtani, K. Sasaki, Importance of ZnTiO3 phase in ZnTi-mixed metal oxide photocatalysts derived from layered double hydroxide, ACS Appl. Mater. Interfaces 12 (2020) 9169–9180.
[54] Z. Wei, F.F. Liang, Y.F. Liu, W.J. Luo, J. Wang, W.Q. Yao, Y.F. Zhu, Photoelectrocatalytic degradation of phenol-containing wastewater by TiO2/g-C3N4 hybrid heterostructure thin film, Appl. Catal. B-Environ. 201 (2017) 600–606.
[55] X. Bai, L. Wang, Y. Wang, W. Yao, Y. Zhu, Enhanced oxidation ability of g-C3N4 photocatalyst via C60 modification, Appl. Catal. B 152–153 (2014) 262–270.
[56] C. Chuaicham, R.R. Pawar, S. Karthikeyan, B. Ohtani, K. Sasaki, Fabrication and characterization of ternary sepiolite/g-C3N4/Pd composites for improvement of photocatalytic degradation of ciprofloxacin under visible light irradiation, J. Colloid Interface Sci. 577 (2020) 397–405.
[57] Y. Yang, J. Li, T. Yan, R. Zhu, L. Yan, Z. Pei, Adsorption and photocatalytic reduction of aqueous Cr(VI) by Fe3O4-ZnAl-layered double hydroxide/TiO2 composites, J. Colloid Interface Sci. 562 (2020) 493–501.
[58] C. Chen, H. Zeng, J. Xiong, S. Xu, D. An, Z-scheme AgBr@Ag/CoAl layered double hydroxide heterojunction for superior photocatalytic Cr(VI) reduction under visible light, Appl. Clay Sci. 192 (2020), 105627.
[59] X. Yuan, Q. Jing, J. Chen, L. Li, Photocatalytic Cr(VI) reduction by mixed metal oxide derived from ZnAl layered double hydroxide, Appl. Clay Sci. 143 (2017) 168–174.
[60] S. Patnaik, K.K. Das, A. Mohanty, K. Parida, Enhanced photo catalytic reduction of Cr (VI) over polymer-sensitized g-C3N4/ZnFe2O4 and its synergism with phenol oxidation under visible light irradiation, Catal. Today 315 (2018) 52–66.
[61] M. Shirzad-Siboni, M. Farrokhi, R. Darvishi Cheshmeh Soltani, A. Khataee, S. Tajassosi, Photocatalytic Reduction of Hexavalent Chromium over ZnO Nanorods Immobilized on Kaolin, Ind. Eng. Chem. Res. 53 (2014) 1079–1087.
[62] Q.P. Wu, J. Zhao, G.H. Qin, C.Y. Wang, X.L. Tong, S. Xue, Photocatalytic reduction of Cr(VI) with TiO2 film under visible light, Appl. Catal. B-Environ. 142 (2013) 142–148.
[63] L. Charlet, C. Tournassat, Fe(II)-Na(I)-Ca(II) cation exchange on montmorillonite in chloride medium: evidence for preferential clay adsorption of chloride – metal ion pairs in seawater, Aquat. Geochem. 11 (2005) 115–137.
[64] Y.L. Ma, Z.R. Xu, T. Guo, P. You, Adsorption of methylene blue on Cu(II)-exchanged montmorillonite, J. Colloid Interface Sci. 280 (2004) 283–288.
[65] J. Kielland, Individual activity coefficients of ions in aqueous solutions, J. Am. Chem. Soc. 59 (1937) 1675–1678.
[66] J.K. Yang, S.M. Lee, Removal of Cr(VI) and humic acid by using TiO2 photocatalysis, Chemosphere 63 (2006) 1677–1684.
[67] D.J. Zhong, J.F. Zhang, Y. Li, X.D. Xie, Adsorption and photocatalytic removal of chromium on high-index TiO2 facet, Huan jing ke xue= Huanjing kexue 40 (2019) 701–707.
[68] J.K. Yang, S.M. Lee, M. Farrokhi, O. Giahi, M.S. Siboni, Photocatalytic removal of Cr(VI) with illuminated TiO2, Desalin. Water Treat. 46 (2012) 375–380.
[69] A. Keri, R. Dahn, M. Krack, S.V. Churakov, Combined XAFS spectroscopy and Ab initio study on the characterization of iron incorporation by montmorillonite, Environ. Sci. Technol. 51 (2017) 10585–10594.
[70] D.G. Costa, A.B. Rocha, W.F. Souza, S.S.X. Chiaro, A.A. Leitão, Comparative structural, thermodynamic and electronic analyses of ZnAlAn− hydrotalcite-like compounds (An−Cl−, F−, Br−, OH−, CO32− or NO3−): an ab initio study, Appl. Clay Sci. 56 (2012) 16–22.
[71] O. Andreussi, I. Dabo, N. Marzari, Revised self-consistent continuum solvation in electronic-structure calculations, J. Chem. Phys. 136 (2012), 064102.
[72] W.M. Haynes, CRC Handbook of Chemistry and Physics, 93rd Edition, Taylor & Francis, 2012.